Scalable Total Synthesis of Portimine A and B Reveals the Basis of Their Potent and Selective Anti-cancer Activity

Junchen Tang*, Weichao Li*, Tzu-Yuan Chiu, Zengwei Luo, Christine T. Chong, Qijia Wei, Francisco Martínez-Peña, Nathalia Gazaniga, Yi Yang See, Luke L. Lairson , Christopher G. Parker† and Phil S. Baran†

*These authors contributed equally to this work.
†Correspondence to: cparker@scripps.edu, pbaran@scripps.edu

ABSTRACT: Marine derived cyclic imine toxins, portimine A and B, have attracted extensive attention owing to their intriguing chemical structure and promising anti-cancer therapeutic potential. However, access to large quantities is currently unfeasible and the molecular mechanism behind their potent activity is unknown. To address this, a scalable 15-step total synthesis of portimines is presented, which benefits from the logic used in two-phase terpenoid synthesis along with unique tactics such as exploiting ring-chain tautomerization and skeletal reorganization to minimize protecting group chemistry through "self-protection". Critically, this total synthesis enabled a structural reassignment of portimine B and an in-depth functional evaluation of portimine A, revealing that it induces apoptosis selectively in human cancer cell lines with high potency. Finally, practical access to the portimines and analogs thereof simplified the development of photoaffinity analogs, which were used in chemical proteomic experiments to identify a primary target of portimine A as the 60S ribosomal export protein NMD3.

For decades, cyclic imine (CI) toxins have stimulated extensive interest from the broad scientific community based on their unique and potent bioactivity coupled with their captivating chemical structures (*1,2*). The therapeutic potentials of larger members in this family, such as pinnatoxins (*3*), spirolides (*4*), and gymnodimines (*5*), have been thwarted by their high neurotoxicity *in vivo*. More compact members of this family were isolated from benthic dinoflagellate *Vulcanodinium rugosum* in 2013 and 2018, portimine A (PA, **1**) and B (PB, **2**) respectively (Fig. 1, absolute configuration confirmed in 2019) (*6–8*). In sharp contrast to classic CI toxins, preliminary reports indicate that **1** is highly cytotoxic (~3 nM) and induces apoptosis in several cancer cell lines, while also displaying lower acute toxicity in mice relative to other shellfish toxins, highlighting its potential as a therapeutic agent (*6*, *9–12*). However, the mechanism of action (MoA) behind its potent activity is unknown. The Achilles heel of such a compound is of course scalable access to its complex architecture. As it is derived from a dinoflagellate in low yield (*6*), chemical synthesis appears to be the only means of realistically procuring such molecules. Even if a bioengineered synthesis could be achieved, semi-synthetic analogs with deep-seated modifications would be unworkable. Featuring a spiro-fused five-membered cyclic imine embedded in a highly oxidized all-carbon tricyclic macrocyclic core, **1** and **2** are formidable targets for synthesis. The unusual peripheral oxidations such as that adjacent to imine carbon (C-5) and neighboring labile medium-sized cyclic ketal add to this challenge. In this work, the first total synthesis of **1** and **2** is presented, which features a carefully choreographed sequence to rapidly build up a minimally oxidized carbon framework followed by strategic oxidations and ring-chain isomerizations that minimize concession steps. In addition, this practical synthesis enabled elaborated *in situ* investigations as well as illumination of the cellular targets of **1** *via* chemical proteomics, revealing that **1** targets the 60S ribosomal export protein NMD3 and blocks polysome formation.

Historically, CI toxins have been constructed by patterning the retrosynthetic analysis on the presumed biogenesis (*13–15*), wherein an acyclic structure with maximum functionality is subjected to macrocyclization (*16–20*). This pioneering approach was first accomplished by Kishi et al. in the 1998 total synthesis of pinnatoxin A (*16*). In the case of the portimines, approaches thus far have followed this dogma (*21–24*). Thus, Brimble *et al.* (*22*, *23*) and Harran *et al.* (*24*) aimed for a bio-inspired synthesis that mimics

the polyketide synthases (PKSs), featuring bold intramolecular cyclizations of densely functionalized polyketides **3** and **4** respectively (Fig 1A). The former approach demonstrated that the ketalization of linear **3** was not facile, even with the well-functionalized skeleton. The latter cycloaddition-based approach resulted in undesired regioselectivity in the pivotal cyclization of **4** to **6**. The difficulty encountered in these routes points to the challenge of forging key bonds in such a densely functionalized polycyclic alkaloid from an acyclic precursor. From a high level, this scenario is not unlike that encountered in the synthesis of densely functionalized, highly oxidized terpene natural products. In those cases, it has been shown that a two-phase approach to synthesis can be beneficial by building up a minimally oxidized carbon framework followed by strategic late-stage oxidations (*25*, *26*).

By analogy to the logic of two-phase synthesis, a minimally oxidized macrocyclic intermediate to the portimines was targeted with the assumption that a proper choreography of oxidation events would solve both connectivity and stereochemical issues. The only C–O bonds to be installed at the outset were those residing at C-4 (imine carbon) and C-10 (secondary alcohol). A triple bond on C-7/8 would be a surrogate for the eventual C-7 oxidation and, critically, offer a strategic disconnection to the macrocycle using ring-closing alkyne metathesis (RCAM) (*27*). Such a tactic would thereby minimize unstable functional groups and redundant redox manipulations since four key oxidations (C-5, C-13, C-14, C-15) would occur post-macrocyclization. To minimize protecting groups (PGs), the innate reactivity and conformational preferences are utilized via ring-chain reorganization/reconstitution steps. Upon unraveling the macrocycle, the dialkynated precursor (**7**) traces back to accessible building blocks (Fig. 1B). Finally, in order to maximize access to useful analogs, a vinyl triflate was selected as a key functionality to be carried through the entire synthesis.

The synthesis is outlined in Fig. 2 and commences with a scalable, asymmetric Diels-Alder cycloaddition (*28*), which established the C-3 chirality. Reduction of C-4, followed by removing the carbamate auxiliary with TBAF, afforded **10** in 88% yield, and 94% ee on 50-gram scale. The requisite methyl-capped alkyne side chain can be installed via a sequence including Grignard addition and two oxidations, delivering **11** as the final product in 60% yield after a single purification. Treatment of **11** with TFA in CH_2Cl_2 afforded spirocyclic imine **12** in 72% yield on gram scale.

The synthesis of fragment **13** was carried out from inexpensive (*S*)-solketal (*ca.* $1.1/g, see the SI for details). To affix this subunit onto the established chiral spirocyclic core **12**, a stereoselective Cu-mediated conjugate addition was applied. The choice of copper (I) reagent (*29*) was crucial since switching to other common copper (I) salts, such as CuI, CuCN, and CuBr, showed little to no observable conversion (Table S2). The stereochemical outcome in this step is controlled by the intrinsic configuration of the spiro-cycle, wherein the side chain blocked the top face. Direct treatment of the *in situ* generated enolate with Comins' reagent ensured the correct regiochemical olefin outcome and smoothly delivered vinyl triflate **7** as a single product (6.5-g scale), which possessed all skeletal carbon atoms required for **1** and **2**.

Attention was then turned to constructing the 14-membered macrocycle in portimines' skeleton through RCAM, a maneuver that might be derailed by the imine, olefins, or vinyl triflate. Fürstner's extremely efficient, canopy-shaped catalyst, [Mo] was chosen at this point due to its outstanding functional compatibility and demonstrated robustness (*30*). The pivotal RCAM step could indeed be achieved in 53-65% yield when heated **7** with [Mo] in toluene. However, a relatively high catalyst loading (12.5 mol %) was required, presumably due to the basic imine nitrogen. To lower the catalyst loading, the imine was masked with a Troc group, followed by exposing the formed enamide to 2.0 mol % [Mo]. In this case, formation of macrocycle **14** was completed in one hour. Treating crude **14** with acidic wet methanol liberated the C-4 ketone and deprotected the TBS ether on C-10, affording **15** as a white powder (68% overall isolated yield over 2 steps, multigram-scale).

Arrival at macrocycle **15** (the end of the "cyclase phase") was a milestone since all requisite core C–C bonds were in place to arrive at **1** and **2**. All that remained was installation of five oxygen atoms at C-5, C-7, C-13, C-14, and C-15. The "oxidase-phase" commenced with oxidation of C-14/15 since olefin-oxidations are well-known to be compatible with alkynes. Initial attempts using oxidants (*i.e.*, OsO_4, *m*-CPBA, etc.) delivered undesired stereochemical outcome at C-15 in all cases (Fig. S2). Therefore, a net six-electron oxidation catalyzed by ruthenium was chosen to arrive at a diketone (*31*), with an eventual strategic reduction to set the desired stereochemistry. Stronger oxidants of this type, however, will not tolerate the presence of an alkyne. For this purpose, an internal protection strategy was designed and achieved upon skeletal reorganization by refluxing **15** and $XPhosAuNTf_2$ (0.8 mol %) in CH_2Cl_2. The newly-formed tricyclic system reorganized all potentially sensitive sites (nitrogen on C-1, C-4 ketone, C-7-C-8 alkyne, and C-10 alcohol) into their inactive states. Subsequent six-electron oxidation under Ru-catalysis led to diketone **16** in a 53% isolated yield (gram-scale) thereby minimizing reliance on PGs.

With this newly constructed rigid polycyclic system in place, the correct oxidation state and stereochemistry on C-14 and C-15 were installed. Site-specific reduction of C-14 was accomplished using L-selectride, followed by treating the crude material with $NaBH_4$ to afford diol **32** (see the SI), which possessed the desired stereochemistry on C-15. Subsequently, C-14 was selectively returned to the ketone oxidation state with TEMPO/NaOCl. Other oxidants tested for this step showed poor selectivity (Table S3). Remarkably, upon heating crude **17** with zinc powder in acetic acid, the Troc group was dismantled and the polycyclic ring system spontaneously unraveled through ring-chain tautomerization (presumably *via* **18**) to liberate the deoxyportimine triflate **19** in 74% yield on gram-scale.

Only two oxygen atoms, at C-13 and C-5, remained to be installed to complete the synthesis. Both oxidations could be achieved in a single step by treating the crude silyl enol ether of **19** with DMDO to afford a nitrone **20** (73% overall yield). Subsequent heating of **20** in the presence of Ac_2O and TEA presumably triggers a Boekelheide type rearrangement (*32*) to deliver a diacetate (compound **39**, see the SI) as a single diastereomer, followed by regioselective hydrolysis of the C-5 acetate using LiOH to yield monoacetate **21** (64%) on 330-mg scale. At this point, the vinyl triflate which had remained a silent observer throughout the synthesis was now called upon to append the final two carbon atoms of **1** and **2**. Thus, a Suzuki coupling was chosen to install the exocyclic vinyl group, delivering diene **22** in 75% yield. To complete the synthesis, **22** was oxidized with DMP, followed by hydrolysis, affording portimine B (PB, **2**) in 88% yield. During these studies we suspected that the originally assigned structure of **2** as a ring-opened tautomer was incorrect and this was now confirmed to be the same ring-closed tautomer expressed in **1**. To complete the synthesis of portimine A (PA, **1**), crude **2** in methanol could be stereoselectively reduced by $NaBH_3CN$ in high isolated yield (80%).

With this scalable synthesis in hand, we next turned to determining the mechanism of action (MoA) of PA (**1**). First, we sought to identify sites that could accommodate a "fully functionalized" retrieval tag to facilitate chemical proteomic target identification while not interfering with the biological activity of the parent structure (*33–38*). Here, an evaluation of portimine A analogs with modifications at multiple sites (Fig. S4A) in Jurkat (human T lymphocyte) and HCC1806 (human breast cancer) cells confirmed that fully-synthetic PB (**2**) showed significantly less toxicity in both cancer cell lines compared to PA (**1**) (7), as did epi-portimine A (ePA, **38**), the C-5 epimer of PA (**1**). Taken together, these results suggests that the anti-proliferative activity of PA (**1**) is dependent on the stereochemistry of C-5, and that ePA (**38**) could be employed as an inactive control compound for further studies. We also noted that phenyl-derivative Ph-PA (**36**) showed similar activity to PA (**1**) in both cell lines, indicating the terminal vinyl group (C-21/22) is not essential for the observed biological activity. Based on these results, we pursued the assembly of a diazirine-alkyne (DA) containing photoaffinity tag at the C-18 position of PA (**1**) through Suzuki coupling with the key intermediate (compound **21**, for detailed synthesis steps, see SI). Encouragingly, we observed both the epimeric photoaffinity probes PA-DA (**35-2**) and ePA-DA (**35-1**) retained

identical activities as their parent analogs, suggesting that they could serve as target ID tools (Fig. 3A-3B).

It had previously been reported that isolated PA (**1**) induces cellular apoptosis (*6, 7*). Indeed, we observe that fully synthetic PA (**1**) also induces apoptosis, as does Ph-DA (**36**) and PA-DA (**35-2**), at low nanomolar concentrations, as determined by caspase-3 activation in Jurkat cells, however controls ePA (**38**) and ePA-DA (**35-1**) do not (Fig. 3C and Fig. S4B). Further investigation also revealed that PA (**1**) and PA-DA (**35-2**) markedly increased the proportion of Jurkat cells in G1 phases (Fig. 3D and Fig. S5A-5B), but not in ePA (**38**) and ePA-DA (**35-1**) treated cells. Notably, we observe that PA (**1**) and Ph-PA (**36**) display minimal effects on cell viability in freshly isolated human peripheral blood mononuclear cells (PBMCs) as well as no obvious effects on caspase activation (Fig. 3E and Fig. S6A-6B), suggesting that their toxicity mechanisms are selective to rapidly proliferating cells.

We next pursued identification of the protein targets of PA (**1**) in cells by tandem mass tags (TMT)-based proteomics (*35*, *39*, *40*). Specifically, we aimed to identify proteins that were substantially enriched (>2-fold) by PA-DA over ePA-DA and competed (>5-fold) by PA (**1**) but not the inactive epimer ePA (**38**) (Fig. 4A-B and Fig. S7A-7F, Table S6-S7) in both Jurkat and HCC1806 cells. We identified only one protein, 60s ribosomal export protein NMD3 in both cell lines that fulfilled these criteria. We verified this interaction by chemoprecipitation (ChP), where the labeling of endogenous NMD3 by PA-DA (**35-2**) could be blocked by excess PA (**1**), but not excess ePA (**38**), and little to no labeling was observed in the absence of UV irradiation or with ePA (**38**) (Fig. 4C and Fig. S7G), suggesting that PA (**1**) selectively and non-covalently binds to NMD3 in cells. NMD3 is an adaptor of 60S ribosomal subunit nuclear export and is released upon pre-60S maturation in the cytosol and subsequent polysome formation, though the precise mechanism of this regulation is not fully elucidated (*41–43*). Notably, we observed that NMD3-deficient Jurkat and HeLa cells were less prone to the cytotoxic effects of PA (**1**), compared to control cells (Fig. 4D-4E, Fig. S8A-8C), suggesting that NMD3 is necessary for its activity. As NMD3 is required for nascent 60S ribosome maturation (*41*), we next examined whether PA (**1**) affects ribosome assembly. Here, we observed that in Jurkat cells treated with PA (**1**), but not inactive ePA (**38**), led the accumulation of 80S monosomes and disomes as well as the blockade of polysome formation (Fig. 4F, Fig. S8D). Further, we observed that eukaryotic translation initiation factor 6 (eIF6), an essential factor of 60S maturation and 80S assembly which is reported to be modulated by NMD3 (*44-46*), is localized in the 60S fraction and decreased in RNA-free fractions in cells treated with PA (**1**) (Fig. 4F, Fig. S8E). Together, these data suggest that PA (**1**) engages NMD3, which results in increased 60S associated eIF6, stabilization of 80S, and subsequent impairment of polysome formation (Fig. 4F), likely leading to cell cycle arrest and apoptosis (*47–49*).

The scalable total synthesis of portimine A (**1**) and B (**2**) presented herein benefits from a strategy that is distinct from both biosynthesis and prior approaches. Driven by a desire to avoid an abundance of functional group manipulations, non-strategic redox fluctuations, and PGs, a plan was forged to forego the installation of oxygenation until a late stage. By analogy to two-phase terpenoid synthesis, this required the construction of a minimally decorated carbon skeleton followed by sequential oxidations. In this way, the innate reactivity of a macrocycle could be leveraged to install both the correct oxygenation pattern as well as the stereochemistry. Certain intermediates served to "self-protect" key functional groups and enable the final sequence by strategically timed ring-chain tautomerization events. Finally, an unusually stable vinyl triflate was carried through the majority of the synthesis allowing for flexible diversification of this biologically promising lead compound, enabling the construction of photoaffinity probes for target identification studies. With sizable quantities of PA (**1**) in hand, we have shown that PA (**1**) potently induces G1 cell cycle arrest and apoptosis in multiple human cancer cell lines, but not in human PBMCs. Further, chemical proteomic studies revealed NMD3 to be the primary target of PA (**1**), and to our knowledge, is the first reported small molecule ligand of NMD3. Engagement of NMD3 by PA results in a buildup of 80S ribosome and blockade of polysome formation. Further, the observation that decreasing NMD3 expression reduces PA potency is suggestive of a gain-of-function or *neo*-function mechanism,

however, the molecular details of how binding of PA (**1**) to NMD3 induces this cascade are not yet clear and will be subject of future studies. Overall, this study demonstrates the utility of totally synthetic routes designed with ideality criterion combined with powerful chemical proteomic methods to reveal new potential therapeutic targets (*50*).

ASSOCIATED CONTENT

Experimental procedures and NMR spectra

Figs. S1 to S8

Tables S1 to S7

AUTHOR INFORMATION

Corresponding Author

E-mail: cparker@scripps.edu, pbaran@scripps.edu

Funding Sources

Financial support for this work was provided by NIGMS (GM118176)

ACKNOWLEDGMENT

We thank Prof. J. Williamson and Dr. A. Popova (Scripps Research) for their invaluable discussions and generous technical assistance with polysome profiling experiments. We are grateful to Dr. D.-H. Huang and Dr. L. Pasternack (Scripps Research) for NMR spectroscopic assistance, Ms. B. Sanchez, Ms. Q. N. Wong, and CoreService Team (Scripps Research) for analytical support. Prof. A. Fürstner and Dr. J. Hillenbrand (Max-Planck-Institut für Kohlenforschung) for providing RCAM catalysts.

AUTHOR CONTRIBUTIONS:

Conceptualization: JT, WL, CGP, PSB

Methodology: JT, WL, TC

Investigation: JT, WL, TC, ZL, CTC, QW, FMP

Funding acquisition: CGP, PSB

Project administration: CGP, PSB

Supervision: LLL, CGP, PSB

JT, WL, CGP and PSB wrote the manuscript.

REFERENCES AND NOTES

(1) C. E. Stivala, E. Benoit, R. Aráoz, D. Servent, A. Novikov, J. Molgó, A. Zakarian, Synthesis and biology of cyclic imine toxins, an emerging class of potent, globally distributed marine toxins. *Nat. Prod. Rep.* **32**, 411–435 (2015). doi:10.1039/c4np00089g

(2) J. Molgó, P. Marchot, R. Aráoz, E. Benoit, B. I. Iorga, A. Zakarian, P. Taylor, Y. Bourne, D. J. Servent, Cyclic imine toxins from dinoflagellates: A growing family of potent antagonists of the nicotinic acetylcholine receptors. *J. Neurochem.* **142**, 41–51 (2017). doi:10.1111/jnc.13995

(3) R. Munday, A. I. Selwood, L. Rhodes, R. Acute toxicity of pinnatoxins E, F and G to mice. *Toxicon*. **60**, 995–999 (2012). doi:10.1016/j.toxicon.2012.07.002

(4) R. Munday, M. A. Quilliam, P. LeBlanc, N. Lewis, P. Gallant, S. A. Sperker, H. S. Ewart, S. L. MacKinnon, Investigations into the toxicology of spirolides, a group of Marine Phycotoxins. *Toxins*. **4**, 1–14 (2011). doi:10.3390/toxins4010001
(5) R. Munday, N. R. Towers, L. Mackenzie, V. Beuzenberg, P. T. Holland, C. O. Miles, Acute toxicity of gymnodimine to mice. *Toxicon*. **44**, 173–178 (2004). doi:10.1016/j.toxicon.2004.05.017
(6) A. I. Selwood, A. L. Wilkins, R. Munday, F. Shi, L. L. Rhodes, P. T. Holland, Portimine: a bioactive metabolite from the benthic dinoflagellate *Vulcanodinium rugosum*. *Tetrahedron Letters*. **54**, 4705–4707 (2013). doi:10.1016/j.tetlet.2013.06.098
(7) A. M. Fribley, Y. Xi, C. Makris, C. Alves-de-Souza, R. York, C. Tomas, J. L. C. Wright, W. K. Strangman, Identification of portimine b, a new cell permeable spiroimine that induces apoptosis in oral squamous cell carcinoma. *ACS Med. Chem. Lett.* **10**, 175–179 (2019). doi:10.1021/acsmedchem-lett.8b00473
(8) I. Hermawan, M. Higa, P. U. B. Hutabarat, T. Fujiwara, K. Akiyama, A. Kanamoto, T. Haruyama, N. Kobayashi, M. Higashi, S. Suda, J. Tanaka, Kabirimine, a new cyclic imine from an okinawan dinoflagellate. *Mar. Drugs* **17**, 353 (2019). doi:10.3390/md17060353
(9) S. L. Cuddihy, S. Drake, D. T. Harwood, A. I. Selwood, P. S. McNabb, M. B. Hampton, The marine cytotoxin portimine is a potent and selective inducer of apoptosis. *Apoptosis* **21**, 1447–1452 (2016). doi:10.1007/s10495-016-1302-x
(10) D. G. Brooke, G. Cervin, O. Champeau, D. T. Harwood, H. Pavia, A. I. Selwood, J. Svenson, L. A. Tremblay, P. L. Cahill, Antifouling activity of portimine, select semisynthetic analogues, and other microalga-derived spirocyclic imines. *Biofouling* **34**, 950–961 (2018). doi:10.1080/08927014.2018.1514461
(11) M. Izumida, K. Suga, F. Ishibashi, Y. Kubo, The spirocyclic imine from a marine benthic dinoflagellate, portimine, is a potent anti-human immunodeficiency virus type 1 therapeutic lead compound. *Mar. Drugs* **17**, 495 (2019). doi:10.3390/md17090495
(12) K. Hogeveen, S. Huet, C. Besnard, J. S. Murray, D. T. Harwood, A. I. Selwood, V. Fessard, In vitro investigation of the genotoxicity of portimine, a cyclic imine toxin produced by the dinoflagellate *Vulcanodinium rugosum*, on human hepatic HepaRG cells. *Toxicol. In Vitro* **73**, 105125 (2021). doi:10.1016/j.tiv.2021.105125
(13) S. L. MacKinnon, A. D. Cembella, I. W. Burton, N. Lewis, P. LeBlanc, J. A. Walter, Biosynthesis of 13-desmethyl spirolide C by the dinoflagellate *Alexandrium ostenfeldii*. *J. Org. Chem.* **71**, 8724–8731 (2006). doi:10.1021/jo0608873
(14) R. Kellmann, A. Stuken, R. J. Orr, H. M. Svendsen, K. S. Jakobsen, Biosynthesis and molecular genetics of polyketides in marine dinoflagellates. *Mar. Drugs* **8**, 1011–1048 (2010). doi:10.3390/md8041011
(15) R. M. Van Wagoner, M. Satake, J. L. Wright, Polyketide biosynthesis in dinoflagellates: what makes it different? *Nat. Prod. Rep.* **31**, 1101–1137 (2014). doi: 10.1039/c4np00016a
(16) J. A. McCauley, K. Nagasawa, P. A. Lander, S. G. Mischke, M. A. Semones, Y.Kishi, Total synthesis of pinnatoxin A. *J. Am. Chem. Soc.* **120**, 7647–7648 (1998). doi: 10.1021/ja981257o
(17) C. E. Stivala, A. Zakarian, Total synthesis of (+)-pinnatoxin A. *J. Am. Chem. Soc.* **130**, 3774–3776 (2008). doi:10.1021/ja800435j
(18) S. Nakamura, F. Kikuchi, S. Hashimoto, Total synthesis of pinnatoxin A. *Angew Chem Int Ed. Engl.* **47**, 7091–7094 (2008). doi:10.1002/anie.200802729
(19) R. Araoz, D. Servent, J. Molgo, B. I. Iorga, C. Fruchart-Gaillard, E. Benoit, Z. Gu, C. Stivala, A. Zakarian, Total synthesis of pinnatoxins A and G and revision of the mode of action of pinnatoxin A. *J. Am. Chem. Soc.* **133**, 10499–10511 (2011). doi:10.1021/ja201254c
(20) K. Kong, Z. Moussa, C. Lee, D. Romo, Total synthesis of the spirocyclic imine marine toxin (-)-gymnodimine and an unnatural C4-epimer. *J. Am. Chem. Soc.* **133**, 19844–19856 (2011). doi:10.1021/ja207385y
(21) T. Saito, K. Fujiwara, Y. Kondo, U. Akiba, T. Suzuki, Synthesis of the cyclohexene segment of portimine. *Tetrahedron Lett.* **60**, 386−389 (2019). doi:10.1016/j.tetlet.2018.12.063

(22) H. R. M. Aitken, M. A. Brimble, D. P. Furkert, A catalytic asymmetric ene reaction for direct preparation of α-hydroxy 1, 4-diketones as intermediates in natural product synthesis. *Synlett* **31**, 687−690 (2020). doi:10.1055/s-0037-1610748

(23) X. B. Ding, H. R. M. Aitken, E. S. Pearl, D. P. Furkert, M. A. Brimble, Synthesis of the C4-C16 polyketide fragment of portimine A and B. *J. Org. Chem.* **86**, 12840−12850 (2021). doi:10.1021/acs.joc.1c01463

(24) L. Li, A. El Khoury, B. O. Clement, C. Wu, P. G. Harran, Asymmetric organocatalysis enables rapid assembly of portimine precursor chains. *Org. Lett.* **24**, 2607−2612 (2022). doi:10.1021/acs.orglett.2c00556

(25) L. Jørgensen, S. J. McKerrall, C. A. Kuttruff, F. Ungeheuer, J. Felding, P. S. Baran, 14-step synthesis of (+)-ingenol from (+)-3-carene. *Science* **341**, 878−882 (2013). doi:10.1126/science.1241606

(26) Y. Kanda, H. Nakamura, S. Umemiya, R. K. Puthukanoori, V. R. Murthy Appala, G. K. Gaddamanugu, B. R. Paraselli, P. S. Baran, Two-phase synthesis of Taxol. *J. Am. Chem. Soc.* **142**, 10526−10533 (2020). doi:10.1021/jacs.0c03592

(27) A. Fürstner, Alkyne metathesis on the rise. *Angew. Chem., Int. Ed.* **52**, 2794−2819 (2013). doi:10.1002/anie.201204513

(28) Y. Huang, T. Iwama, V. H. Rawal, Design and development of highly effective Lewis acid catalysts for enantioselective Diels-Alder reactions. *J. Am. Chem. Soc.* **124**, 5950−5951 (2002). doi:10.1021/ja026088t

(29) E. J. Corey, D. J. Beames, Mixed cuprate reagents of type R_1R_2CuLi which allow selective group transfer. *J. Am. Chem. Soc.* **94**, 7210–7211 (1972) doi:10.1021/ja00775a089

(30) J. Hillenbrand, M. Leutzsch, E. Yiannakas, C. P. Gordon, C. Wille, N. Nothling, C. Coperet, A. Fürstner, "Canopy catalysts" for alkyne metathesis: molybdenum alkylidyne complexes with a tripodal ligand framework. *J. Am. Chem. Soc.* **142**, 11279–11294 (2020). doi:10.1021/jacs.0c04742

(31) S. Chen, Z. Liu, E. Shi, L. Chen, W. Wei, H. Li, Y. Cheng, X. Wan, Ruthenium-catalyzed oxidation of alkenes at room temperature: a practical and concise approach to alpha-diketones. *Org. Lett.* **13**, 2274–2277 (2011). doi:10.1021/ol200716d

(32) C. H. Cummins, R. M. Coates, α-Oxygenation of aldehydes and cyclic ketones by acylation-rearrangement of nitrones. *J. Org. Chem.* **48**, 2070–2076 (1983). doi: 10.1021/jo00160a027

(33) Z. Li *et al.*, Design and Synthesis of Minimalist Terminal Alkyne-Containing Diazirine Photo-Crosslinkers and Their Incorporation into Kinase Inhibitors for Cell- and Tissue-Based Proteome Profiling. *Angew. Chem. Int. Ed.* **52**, 8551-8556 (2013).

(34) C. G. Parker *et al.*, Ligand and Target Discovery by Fragment-Based Screening in Human Cells. *Cell* **168**, 527-541.e529 (2017).

(35) Y. Wang *et al.*, Expedited mapping of the ligandable proteome using fully functionalized enantiomeric probe pairs. *Nature Chemistry* **11**, 1113-1123 (2019).

(36) C. G. Parker, M. R. Pratt, Click Chemistry in Proteomic Investigations. *Cell* **180**, 605-632 (2020).

(37) C. G. Parker *et al.*, Chemical Proteomics Identifies SLC25A20 as a Functional Target of the Ingenol Class of Actinic Keratosis Drugs. *ACS Central Science* **3**, 1276-1285 (2017).

(38) L. P. Conway, W. Li, C. G. Parker, Chemoproteomic-enabled phenotypic screening. *Cell Chemical Biology* **28**, 371-393 (2021).

(39) L. P. Conway et al., Evaluation of fully-functionalized diazirine tags for chemical proteomic applications. *Chemical Science* **12**, 7839-7847 (2021).

(40) G. C. McAlister *et al.*, MultiNotch MS3 Enables Accurate, Sensitive, and Multiplexed Detection of Differential Expression across Cancer Cell Line Proteomes. *Analytical Chemistry* **86**, 7150-7158 (2014).

(41) J. Sengupta *et al.*, Characterization of the nuclear export adaptor protein Nmd3 in association with the 60S ribosomal subunit. *Journal of Cell Biology* **189**, 1079-1086 (2010).

(42) J. H.-N. Ho, G. Kallstrom, A. W. Johnson, Nmd3p Is a Crm1p-Dependent Adapter Protein for Nuclear Export of the Large Ribosomal Subunit. *Journal of Cell Biology* **151**, 1057-1066 (2000).

(43) C. R. Trotta, E. Lund, L. Kahan, A. W. Johnson, J. E. Dahlberg, Coordinated nuclear export of 60S ribosomal subunits and NMD3 in vertebrates. *The EMBO Journal* **22**, 2841-2851 (2003).
(44) M. Ceci et al., Release of eIF6 (p27BBP) from the 60S subunit allows 80S ribosome assembly. *Nature* **426**, 579-584 (2003).
(45) A. G. Malyutin, S. Musalgaonkar, S. Patchett, J. Frank, A. W. Johnson, Nmd3 is a structural mimic of eIF5A, and activates the cpGTPase Lsg1 during 60S ribosome biogenesis. *The EMBO Journal* **36**, 854-868 (2017).
(46) S. Klinge, J. L. Woolford, Ribosome assembly coming into focus. *Nature Reviews Molecular Cell Biology* **20**, 116-131 (2019).
(47) L. M. Lindqvist et al., Translation inhibitors induce cell death by multiple mechanisms and Mcl-1 reduction is only a minor contributor. *Cell Death & Disease* **3**, e409-e409 (2012).
(48) A. Fan, P. P. Sharp, Inhibitors of Eukaryotic Translational Machinery as Therapeutic Agents. *Journal of Medicinal Chemistry* **64**, 2436-2465 (2021).
(49) J. Pelletier, G. Thomas, S. Volarević, Ribosome biogenesis in cancer: new players and therapeutic avenues. *Nature Reviews Cancer* **18**, 51-63 (2018).
(50) D.S. Peters, C. R. Pitts, K. S. McClymont, T. P. Stratton, C. Bi, P. S. Baran, Ideality in Context: Motivations for Total Synthesis. *Acc. Chem. Res.* **54**, 605–617 (2021).

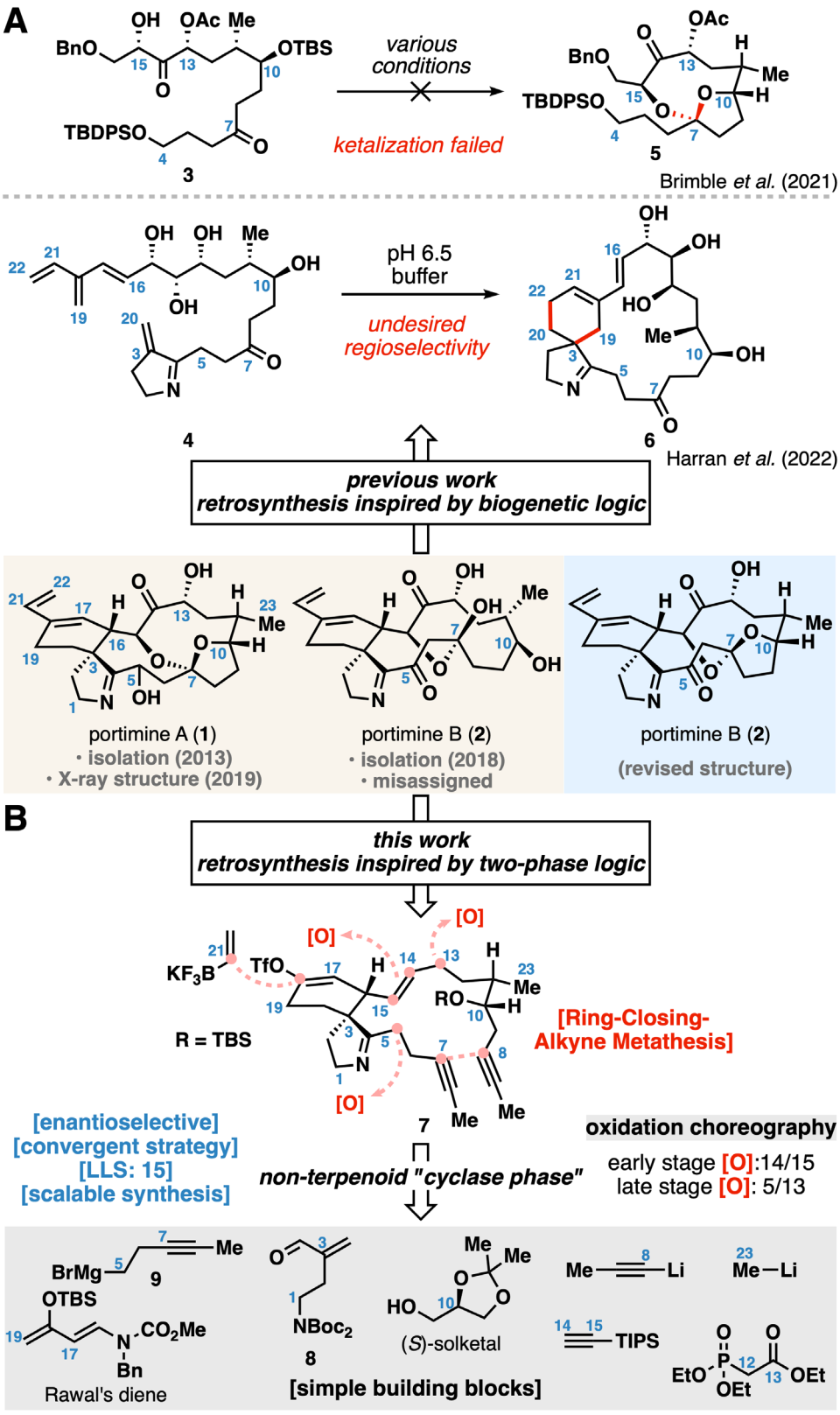

Fig. 1. Previous strategies towards portimines and retrosynthetic analysis in this work.

(**A**) Representative strategies used in previous studies. (**B**) Retrosynthetic analysis in this work. LLS, longest linear sequence.

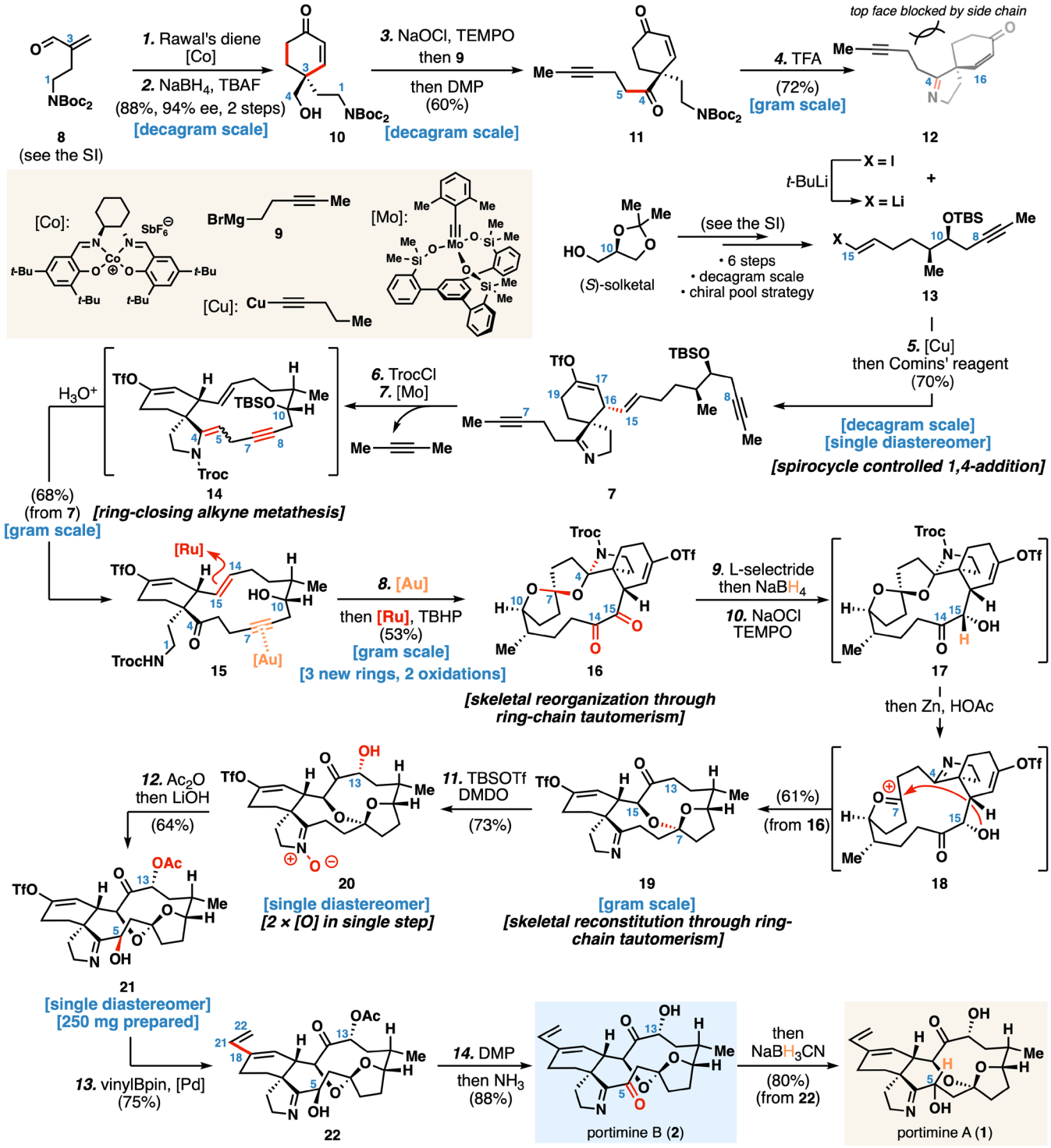

Fig. 2. Total synthesis of portimine A and B.

TEMPO, (2,2,6,6-tetramethylpiperidin-1-yl)oxyl; DMP, Dess–Martin periodinane; TFA, trifluoroacetic acid; TrocCl, 2,2,2-trichloroethoxycarbonyl chloride; TBHP, *tert*-butyl hydroperoxide; TBSOTf, *tert*-butyldimethylsilyl trifluoromethanesulfonate; DMDO, dimethyldioxirane; [Pd], $Pd(dppf)Cl_2 \cdot CH_2Cl_2$, [1,1′-bis(diphenylphosphino)ferrocene]dichloropalladium(II), complex with dichloromethane

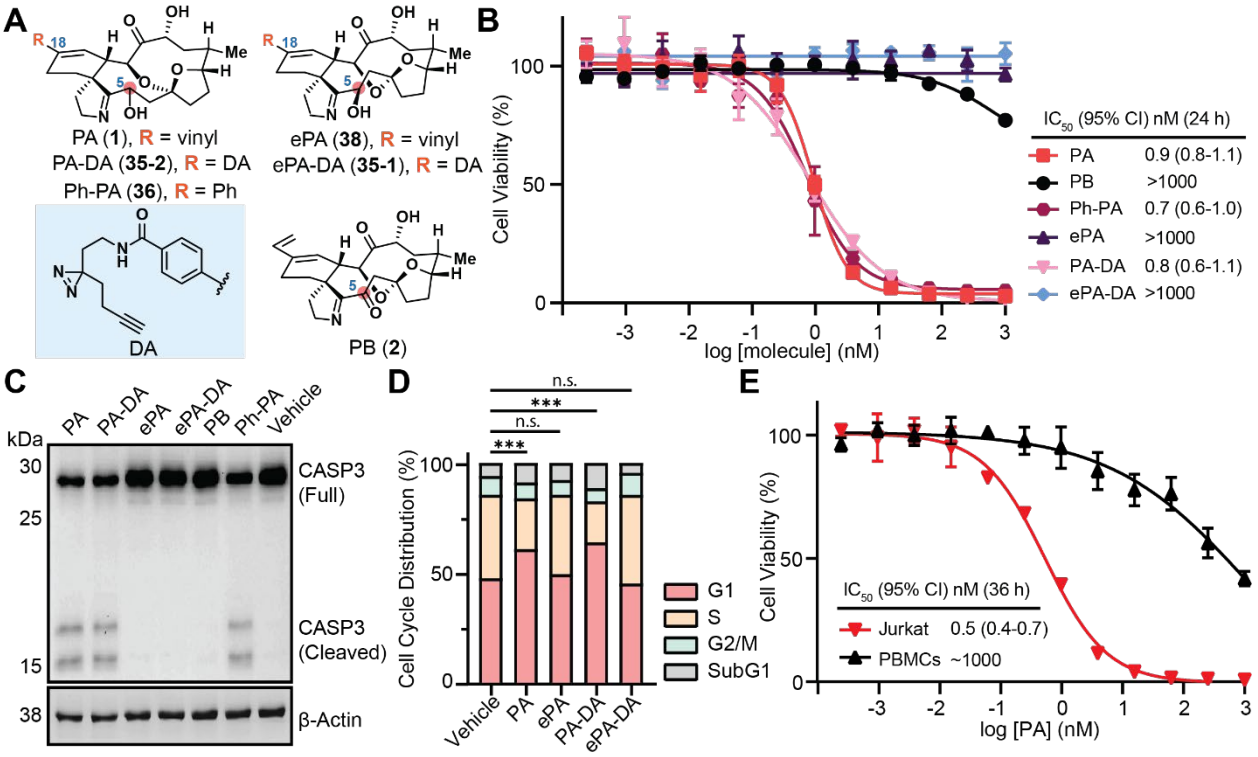

Fig. 3. Portimine A and its functional analogs show stereo-selective acute toxicity in cancer cells.

(**A**) Structure of portimine related analogs: phenyl-portimine A (Ph-PA, **36**) and epi-portimine A (ePA, **38**), portimine A-diazirine-alkyne (PA-DA, **35-2**) and epi-portimine A-diazirine-alkyne (ePA-DA, **35-1**). (**B**) Effects of portimine A and analogs on Jurkat cell viability (24 hrs). All presented data as mean of biological replicated experiments (n = 3). (**C**) Immunoblot of caspase 3 cleavage of Jurkat cells treated with PA, PA-DA, Ph-PA, ePA, ePA-DA and PB (1 nM, 12 hrs). (**D**) PA induce G1-phase arrest. Jurkat cells were treated with portimine A or analogs for 12 hours at 1 nM (n = 3 for each condition). Statistical analysis was performed for G1 phase distribution using multiple unpaired Student t-test, n.s. not significant, *** $p \leq 0.001$. (**E**) PA displays minimal toxicity in freshly isolated human PBMCs (36 hrs). Data presented as mean ± SD.

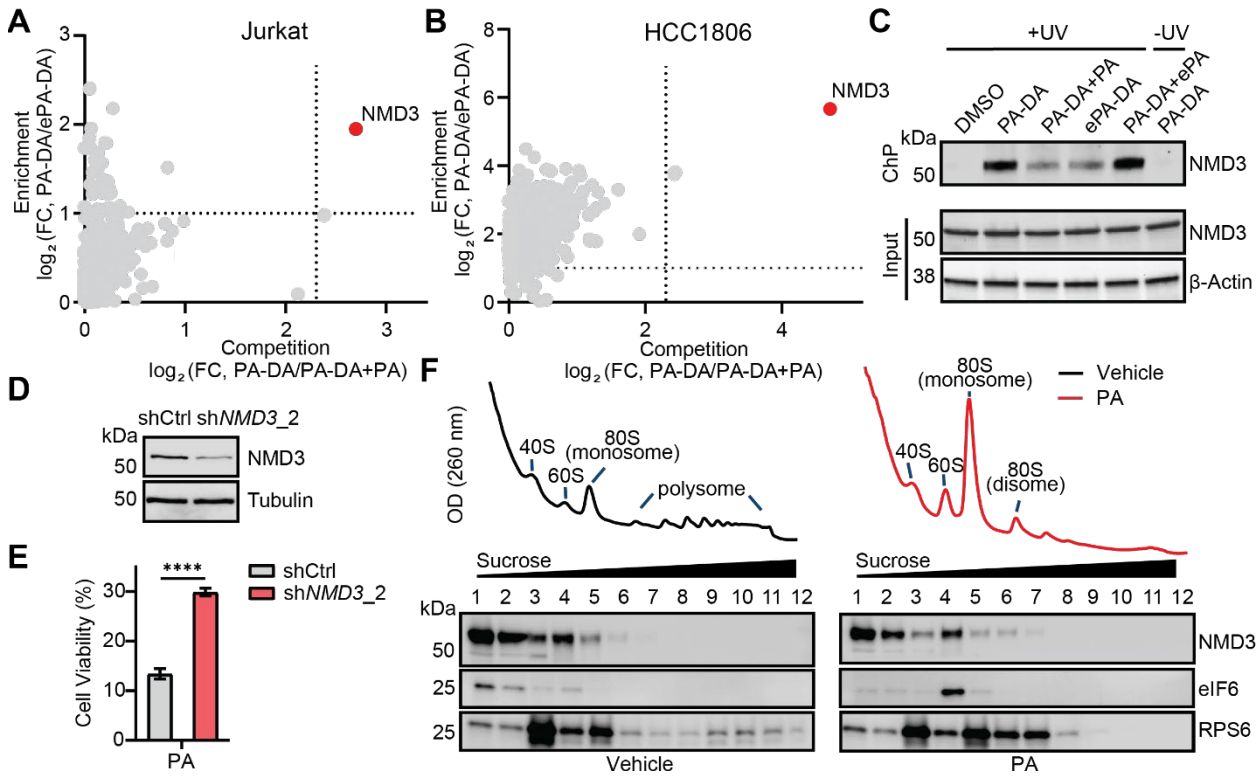

Fig. 4. Portimine A targets NMD3 and prevents polysome formation.

Chemoproteomic profiling of Portimine A in Jurkat (**A**) and HCC1806 cells (**B**). The x-axis shows protein competition in cells treated with active photoaffinity probe PA-DA (500 nM) and DMSO or the active competitor portimine A (PA, 4 μM), while the y-axis shows protein enrichment by active probe PA-DA over inactive photoaffinity probe ePA-DA (500 nM). Proteins designated as PA-specific targets are highlighted in red (competed by active competitor > 5-fold; enriched by PA-DA > 2-fold; and a difference between active and inactive competitors of > 4-fold; all *p*-values < 0.05). Dotted lines indicate active competition (x-axis) and enrichment (y-axis) thresholds. All other points are colored grey. All data presented as mean of biological replicated experiments ($n = 2$). (**C**) Confirmation of PA-DA and PA engagement of endogenous NMD3 in Jurkat cells. (**D**, **E**) PA has reduced viability effects in Jurkat cells transduced with shRNA targeting NMD3 (shNMD3) compared to control cells (shCtrl). (**D**) Immunoblot showing reduced NMD3 levels in shNMD3 Jurkat cells. (**E**) shCtrl and shNMD3 Jurkat cells were treated with 10 nM of PA for 24 hours. (**F**) Representative polysome profiling of Jurkat cells treated with portimine A (6 hr, 50 nM). Cell lysates were fractionated by sucrose gradient and each fraction analyzed by immunoblot. eIF6 levels increase in 60S subunit fraction and polysome marker RPS6 is decreased in polysome fractions after PA treatment. Results are representative of three independent experiments. Statistical analysis was performed using multiple unpaired Student t-test, **** $p \leq 0.0001$.